Polar Stratospheric Cloud Observations at Concordia Station by Remotely Controlled Lidar Observatory

Luca Di Liberto [1], Francesco Colao [2], Federico Serva [3], Alessandro Bracci [1], Francesco Cairo [1] and Marcel Snels [1,*]

[1] CNR-Institute of Atmospheric Sciences and Climate, Via Fosso del Cavaliere 100, 00133 Rome, Italy; l.diliberto@isac.cnr.it (L.D.L.); a.bracci@isac.cnr.it (A.B.); f.cairo@isac.cnr.it (F.C.)
[2] ENEA (Agenzia Nazionale per le Nuove Tecnologie, L'energia e lo Sviluppo Economico Sostenibile), Via Enrico Fermi 45, 00044 Frascati, Italy; francesco.colao@enea.it
[3] CNR-ISMAR (Istitute of Marine Science),Via Fosso del Cavaliere 100, 00133 Roma, Italy; federico.serva@ismar.cnr.it
* Correspondence: m.snels@isac.cnr.it; Tel.: +39-649934316

Abstract: Polar stratospheric clouds (PSCs) form in polar regions, typically between 15 and 25 km above mean sea level, when the local temperature is sufficiently low. PSCs play an important role in the ozone chemistry and the dehydration and denitrification of the stratosphere. Lidars with a depolarization channel may be used to detect and classify different classes of PSCs. The main PSC classes are water ice, nitric acid trihydrate (NAT), and supercooled ternary solutions (STSs), the latter being liquid droplets consisting of water, nitric acid, and sulfuric acid. PSCs have been observed at the lidar observatory at Concordia Station from 2014 onward. The harsh environmental conditions at Concordia during winter render successful lidar operation difficult. To facilitate the operation of the observatory, several measures have been put in place to achieve an almost complete remote control of the system. PSC occurrence is strongly correlated with local temperatures and is affected by dynamics, as the PSC coverage during the observation season shows. PSC observations in 2021 are shown as an example of the capability and functionality of the lidar observatory. A comparison of the observations with the satellite-borne CALIOP (Cloud-Aerosol Lidar with Orthogonal Polarization) lidar has been made to demonstrate the quality of the data and their representativeness for the Antarctic Plateau.

Keywords: climate; ozone; stratosphere; polar stratospheric clouds; lidar

1. Introduction

The first sightings of polar stratospheric clouds were reported in the late 19th century. Because of their brilliant colors, they were called nacreous clouds or mother-of-pearl clouds. Later on, it was discovered that they formed in the stratosphere under very cold conditions.

Only after the discovery of the ozone hole did polar stratospheric clouds gain major attention, being held responsible for catalyzing the ozone destruction by chlorine and bromine. The scientific observation of PSCs started around 1990 with ground-based lidars (McMurdo, Dumont D'Urville, South Pole) and in the 21st century with satellite-borne lidars. From the beginning, two types of PSCs were distinguished, type II, forming below the ice frost point around $-83\,^\circ$C, consisting of water ice and exhibiting the bright colors of mother-of-pearl, and type I, which were also observed at warmer temperatures. The latter were divided into subclasses, with different chemical compositions. One subclass is formed by liquid supercooled particles composed of water, nitric acid, and sulfuric acid (STSs (supercooled ternary solutions)). These particles have spherical symmetry and thus don't depolarize the laser light. A second subclass is formed by water and nitric acid, typically with a stoichiometry of 3:1 (nitric acid trihydrate (NAT)). Both NAT and other nitric acid hydrates are solid particles and thus cause a depolarization of the laser light. Externally mixed clouds with intermediate characteristics are also often observed.

Lidars with a receiver equipped with two detectors to separate polarized and depolarized signals (see, e.g., ref. [1] for a review of polarization lidars) are thus an excellent tool that allows the classification of the different PSC types and subclasses. Ground-based lidars have been active in Antarctica since 1987 and in the Arctic polar regions since 1989. Krüger [2] reported lidar observations at Ny-Aalesund/Svalbard in 1989. The first lidar measurements in Antarctica were reported by Fiocco and coworkers [3], who reported the observation of PSCs at the South Pole station using a laser emitting at 532 nm without a depolarization channel. Stefanutti [4] reported lidar observations at Dumont D'Urville from 1989 to 1993. Recent PSC observations at Dumon D'Urville have been reported in [5]. A polarization lidar was active at McMurdo from 1989 up to 2010 [6,7], and was transferred to Concordia Station in 2014 [8]. A combination of simultaneous lidar and balloon-borne optical particle counter measurements allows the comparison of size distributions with the observed optical properties of aerosol present in PSCs [9,10].

Very few stratospheric lidars have been operating in the Antarctic, and only two of these are primary lidar stations of the Network of Atmospheric Composition Change (NDACC). These are located at Dumont D'Urville and at Concordia Station. In a recent study [11], Concordia Station was identified as one of the best locations for observing polar stratospheric clouds. One reason is the limited cloud cover by cirrus clouds, which might partly block the lidar and reduce the useful range for PSCs. Moreover, Concordia Station is well within the polar vortex during most of the Austral winter, which implies that the conditions for PSC formation are favorable, leading to a frequent occurrence.

Operating a lidar in Antarctica presents additional problems with respect to a lidar at midlatitude locations. This is mainly due to the remoteness of the station and the harsh environmental conditions, which render technical adjustments and maintenance difficult. This is mitigated by the redundancy of the most important components of the lidar, such as the laser and optical systems, as well as the data acquisition modules. Technicians and scientists who run the observatory and many other experiments must be instructed during the summer campaign, and they often have no prior experience with lasers or lidars. However, they are essential for running the system, acquiring data, cleaning the view window, and performing other tasks. During the last few years, lidar alignment and data acquisition have been performed remotely. This implies that the technicians can remain in their office to operate the observatory, without having to go outside at temperatures that can be as low as $-70\ ^\circ\text{C}$ with bad visibility and strong winds to reach the observatory at a distance of 300–400 m. If necessary, the lidar can be remotely controlled from our institute in Italy.

This paper has the following structure. In Section 2, the remotely controlled lidar system is described, followed by a description of the measurement protocols, the preprocessing of the raw data, and the methods to determine the detection and the classification of the PSCs. Subsequently, the results of the observations in 2021 are presented as an example of the PSC observations throughout the years 2014–2023. They will be discussed together with the coincident measurements of the satellite-borne CALIOP lidar. A short overview of the possible formation processes reported in the literature is presented, as well as the strong temperature dependence of PSC formation. The concluding remarks deal with the comparison of ground-based and satellite-borne instruments in general and the detection limits of both systems. Also, the seasonal variation in the observed PSCs will be discussed in relation to the local temperatures measured with radio sondes and integrated with NCEP data.

2. Materials and Methods

2.1. Description of the Remote-Controlled Lidar

Concordia Station is a French–Italian research facility that was built in 2005, located on the Antarctic Plateau at 3233 m above sea level (75.1°S 123.3°E; see Figure 1). Its position is at the Antarctic Plateau, about 1100–1200 km from the French research station at Dumont D'Urville, Australia's Casey Station (see Figure 1), and the Italian Zucchelli Station at Terra

Nova Bay, all of which are coastal stations, making it a unique location for the observation of polar stratospheric clouds. Concordia is operational throughout the year, with a winter staff of about 15 technicians and scientists. At a latitude of 75.1°S, no daylight is present from May through July, and quite spectacular views can be observed when the green laser emission illuminates the sky (see Figure 2).
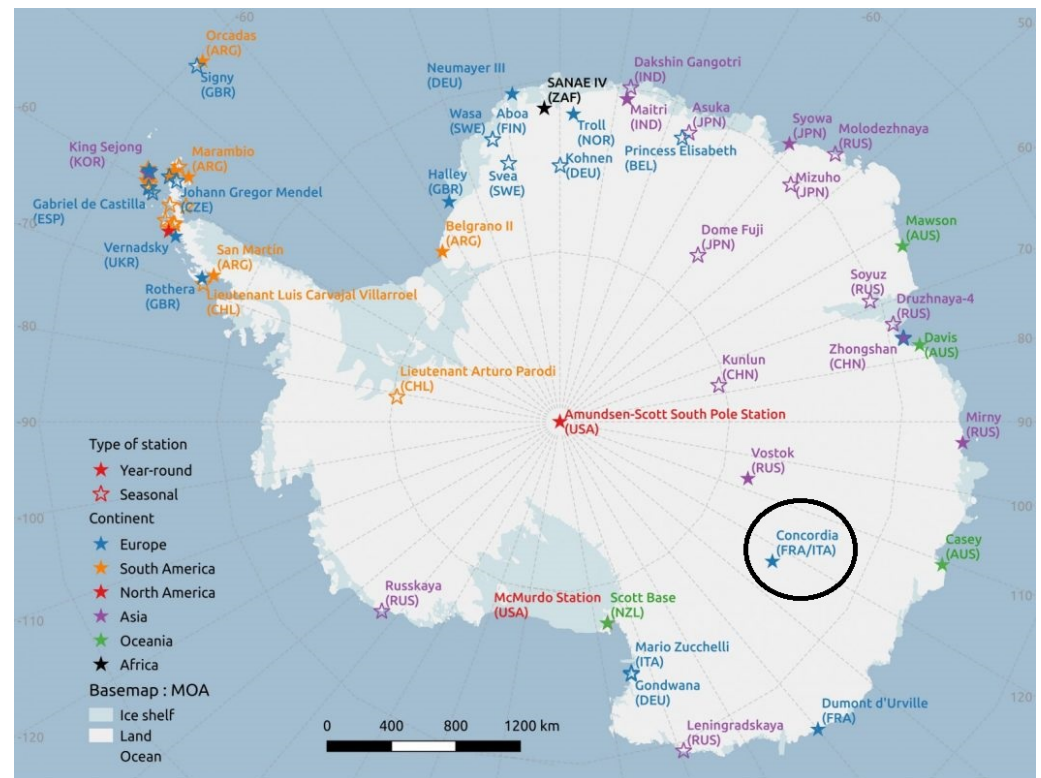

Figure 1. The figure shows a map of Antarctica. The position of Concordia Station with respect to other bases is indicated with a black circle.
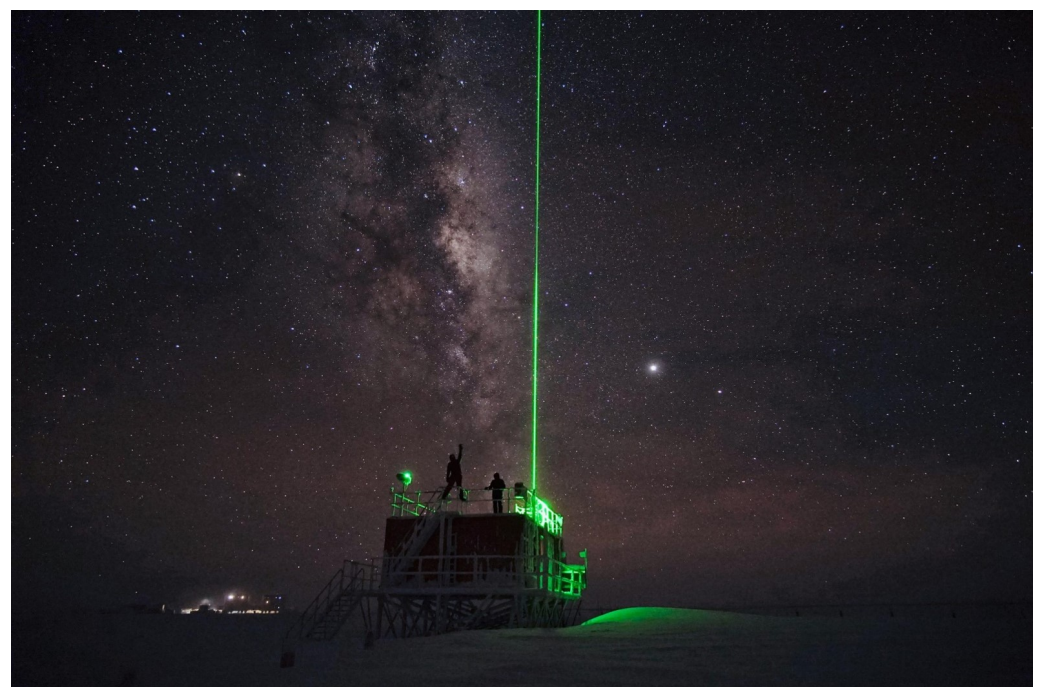

Figure 2. The lidar illuminates the polar sky at Concordia Station. Photo courtesy of Luca Ianniello.

The lidar observatory at Concordia Station has been active since 2014. The main equipment was already deployed at McMurdo Station from 2004 to 2010 [7]. However, many components have been upgraded and added to increase the reliability and redundancy of the instruments. The substitution of the laser and the photon-counting electronics improved the data quality and extended the measurement range. The remote control of data acquisition, the setting of system parameters, and laser alignment have been implemented in the last four years. The lidar observatory uses a compact Quantel Big Sky laser (model CFR400) emitting at two wavelengths at a 10 Hz repetition rate, with a pulse energy of about 180 mJ at 532 nm and 100 mJ at 1064 nm. Two receivers are used to collect the scattered light. A Schmidt Cassegrain telescope (Celestron model C14-AF XLT) with a diameter of 14 inches (355.6 mm) is used for the observation of PSCs at ranges between 10 and 30 km, while a smaller 6-inch (152.4 mm) telescope (Celestron model C6S GT XLT) is used to observe tropospheric clouds. The larger receiver is coupled to an optical box where the optical signal is separated into different components and detected by miniaturized photomultipliers (Hamamatsu models H6780-20, H5783P, and H10721P-210) for the optical wavelengths or by an avalanche photodiode (APD, EG&G, Perkin-Elmer model SPCM-AQR-14) for the infrared signal. Details of the optical system can be found in [12]. The most important lidar specifications are displayed in Table 1. The lidar has a bistatic configuration, with a distance of about 30 cm between the laser emission and the axes of both telescopes (see Figure 3). The laser emission is directed vertically with a piezo-controlled mirror with two axes of freedom, while the main telescope is static. The smaller telescope has a computer-controlled mechanical angular movement, which allows it to vary its axis with respect to the laser emission.
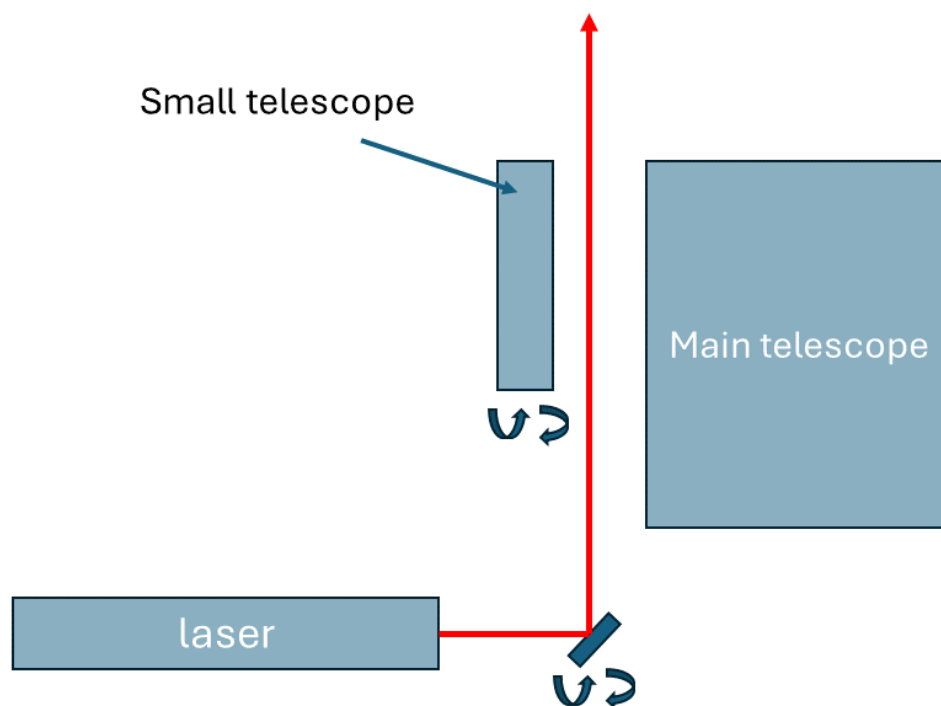

Figure 3. The bistatic configuration is schematically shown. The laser emission is directed vertically with a piezo-controlled mirror with two axes of freedom, while the main telescope is static. The smaller telescope has a two-dimensional computer-controlled mechanical movement, which allows it to vary its axis with respect to the laser emission.

Table 1. Lidar specifications.

Laser energy per pulse	180 mJ
Pulse repetition frequency	10 Hz
Laser pulse duration	9 ns
Laser divergence full angle	1.5 mrad
Laser pointing stability	100 µrad
Main telescope diameter	355.6 mm
Main telescope focal length	3910 mm
Main telescope field of view	4 mrad
Small telescope diameter	152.4 mm
Small telescope focal length	1500 mm
Small telescope field of view	2 mrad
FWHM interference filter @ 532 nm	2 nm

The output of the optical detectors is fed into a photon-counting system (ALA Systems, model APC26 main) with ten available channels, offering some redundancy for the 7 detectors. The parameters of the photon-counting system, including dwell time, number of averages, and pretrigger, among others, can be remotely controlled and the lidar profiles are automatically stored on a local computer and transmitted to a dedicated server in Italy. A script on this server checks every 30 min if new data are available and provides a quick view of the raw data, allowing one to check if the lidar is functioning properly. The local computer can be accessed remotely and allows the control of the laser, the photon-counting system, the data storage, and transmission, as well as control of the laser alignment.

Since 2018, the lidar system has been equipped with an automated alignment system controlled by the local computer, which can be accessed via a satellite VPN connection. This advanced configuration allows control and alignment of the complete system at Concordia Station independently of the weather conditions. The remote control procedures have been designed to control system parameters and to verify and optimize the alignment of the lidar. Initially, the laser emission is aligned almost parallel with the axis of the main telescope with a slight tilt towards the telescope. In this way, the laser illuminates the field of view of the telescope. Subsequently, the smaller telescope is adjusted to capture the signals produced by the air mass illuminated by the laser emission at low altitudes. Optimal lidar alignment is achieved when the emission of the laser remains within the field of view of the telescopes. The current configuration allows for adjustments of the laser emission with respect to the main telescope by using a piezo-controlled mirror (Newport model AG100), which can be scanned in azimuth and tangent angles with respect to the axis of the large telescope. The alignment procedure involves monitoring the 532 nm polarized (high and low) and depolarized channels for the main receiver, as depicted in Figure 4.

A dedicated computer program in Python provides an automatic alignment procedure by scanning the two angles with respect to a starting point and acquires the lidar signal at each setting, thus creating an intensity map by integrating the amplitude of the return signal (in photon counts) between predetermined altitudes. The maximum signal of this map becomes a new starting point, and the process is repeated until the optimum signal is obtained. Alternatively, the piezo-controlled mirror can be accessed directly by the operator to find the best conditions "manually". Once the laser emission is aligned on the main telescope, the smaller telescope can be aligned on the laser beam by using a similar procedure. In this case, a mechanical movement of the smaller telescope allows it to optimize its field of view with respect to the laser emission. During both procedures, a so-called quality factor, derived from the integrated signals between opportune altitudes, which are different for the large telescope and smaller telescope, since the latter should

cover the troposphere only, is calculated and can be displayed in a 2D graph as a function of the two angles with respect to the telescope. The darkest areas in Figure 5 correspond to the maximum overlap between laser emission and the field of view of the telescope. The alignment procedure for both telescopes is iterated until a satisfactory alignment has been obtained.
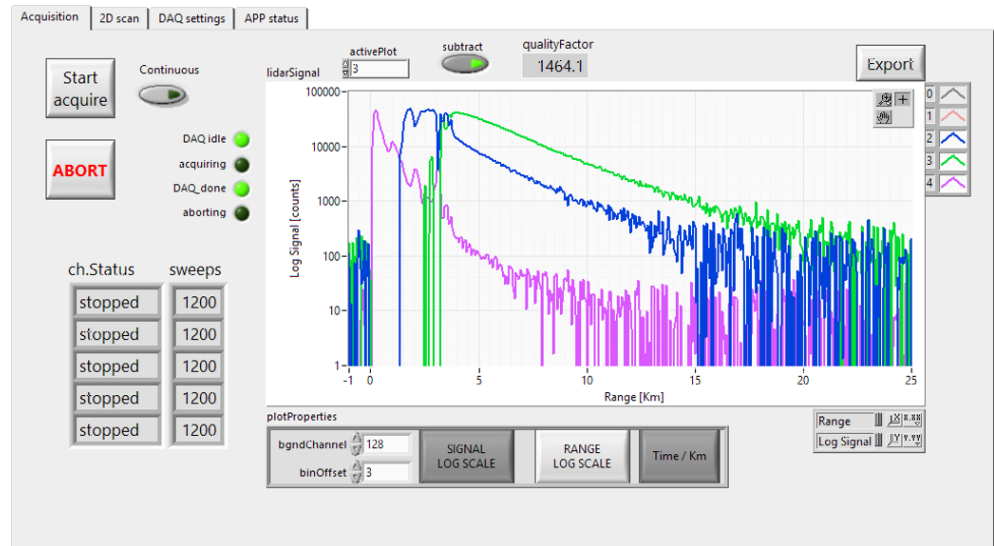

Figure 4. Screenshot of the automatic alignment program, showing the three signals of the 532 nm channels. The vertical axis is in logarithmic scale to display the full dynamics of the signals. The horizontal axis reports the distance from the lidar in km.
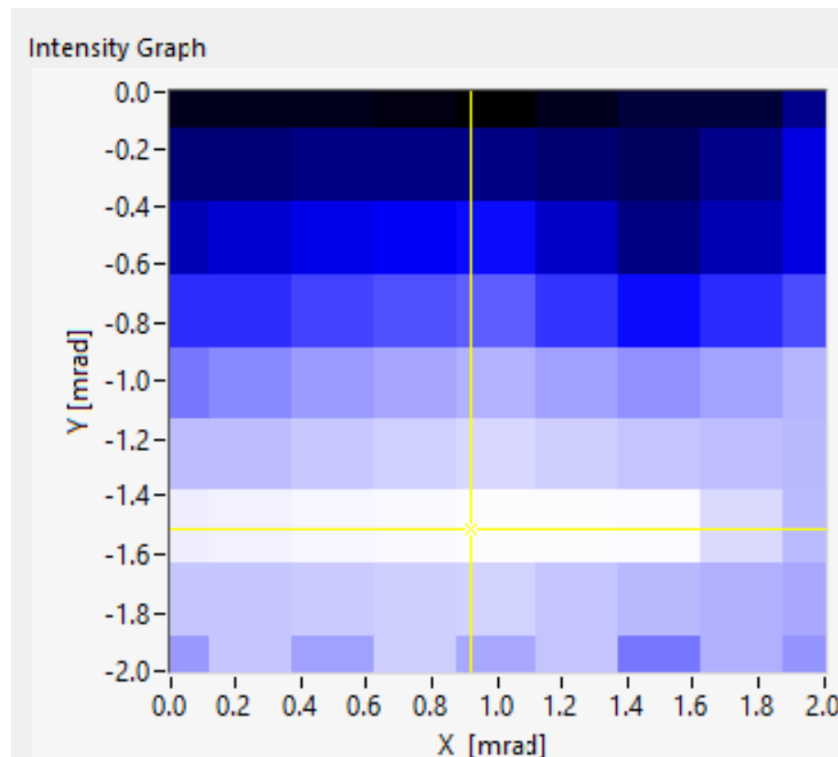

Figure 5. Screenshot of the automatic alignment program showing the intensity map of the received signals in the function of the two angular displacements of the piezo-controlled mirror. The darker colors correspond with the highest-quality factor, representing the maximum overlap obtained for a certain altitude range. The yellow lines define a cursor position and allow to obtain the value of the quality factor in as specific position of the graph.

The laser parameters can be accessed remotely, which allows one to optimize laser intensity and monitor the state of the flash lamps. See Figure 6 for a schematic view of the remotely controlled hardware. A set of remotely controlled power sockets is used to supply current to the computer, laser, and electronics. The local computer, accessible via the internet (VPN), when powered, is booted with a dedicated script and controls the photon-counting electronics, the laser, and the piezo-controlled mirror.
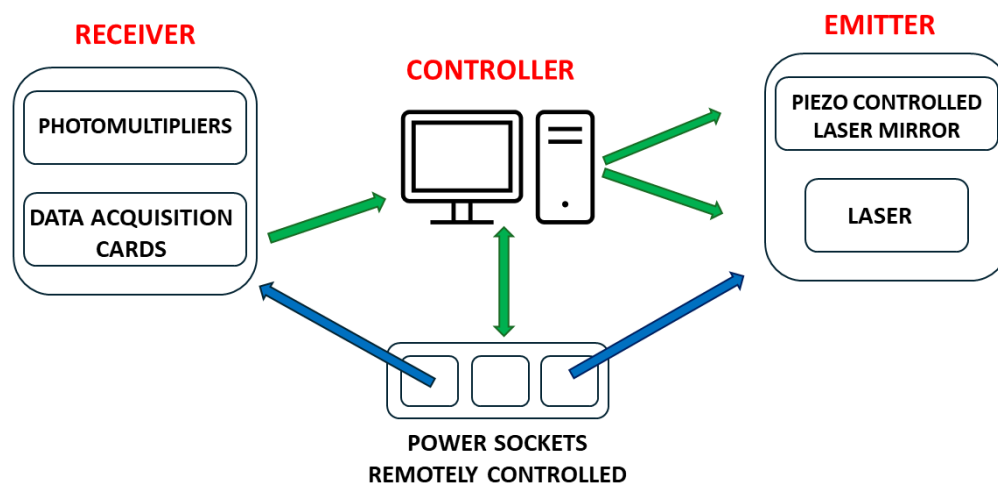

Figure 6. The figure shows a schematic view of the remote control.

2.2. Description of the Measurement Methods

A satellite-borne lidar (CALIOP) on the CALIPSO (Cloud-Aerosol Lidar and Infrared Pathfinder Satellite Observations) satellite was active from 2006 to 2023. CALIPSO was part of the A-train and had an orbit inclination of 98.2°. It provided extensive daily measurement coverage over the polar regions of both hemispheres up to 82° in latitude, with 14 or 15 orbits per day. Most measurements at Concordia Station were made in coincidence with CALIPSO overpasses, having footprints at distances smaller than 300 km from Concordia Station. This results in a few quasi-coincidences per day (see also [7,8]). These coincident measurements allowed the comparison of ground-based and satellite-borne instruments for a large data set of PSC observations. Usually, measurements were performed starting 16 min before the overpass and terminating 16 min after the overpass in intervals of 2 min. These 16 measurements with a duration of two minutes were averaged to improve the signal-to-noise ratio, but they might also be used separately at the cost of a worse signal-to-noise ratio, e.g., to observe variations in the PSC observations on the time scale of minutes, which is useful to obtain information about the extension of PSCs considering the wind speed at different altitudes. Raw data were recorded with photon counting with a dwell time of 400 ns, corresponding with a vertical resolution of 60 m.

2.3. Preprocessing of the Raw Lidar Data

The laser emits linearly polarized light at 532 nm. The molecules and particles in the air may partly depolarize the reflected light. The main constituents of the atmosphere are oxygen and nitrogen molecules, which reflect mainly polarized light, with a small fraction of depolarized light. Particles with spherical symmetry (liquid droplets) do not depolarize the reflected light, while solid particles reflect both polarized and depolarized radiation. Thus, measuring two orthogonal polarizations of the reflected light provides information about the physical (and chemical) properties of the aerosol particles. A set of polarizing beam splitter cubes are used to separate two polarizations, one with a polarization parallel to the emitted laser beam and the second orthogonal to it. Here, we consider the preprocessing of the raw optical signals of the two polarizations (parallel and perpendicular). Both signals are attenuated by the molecules and particles in the air, and a correction is applied to compensate for this attenuation by using a simplified version of the Klett method [13]

that uses a fixed lidar ratio of 70 sr, which appears appropriate for PSCs. We tested this fixed lidar ratio on many lidar profiles and obtained satisfactory results compared with the method proposed by Young and Vaughan [14]. Böckmann and Ritter [15] report a lidar ratio of 55–60 sr for PSCSs at 532 nm, while Gobbi et al. [16] found a maximum value of 70 sr for the lidar ratio at 532 nm from their simulation for ice and NAT PSCs (run 86). The variable lidar ratio used in previous work [12], using the results of a number of model calculations for several particle size distributions [16] (runs 86 and 99) produced less satisfactory results, leading to a significant underestimation of the extinction.

Unfortunately, the two recorded channels with orthogonal polarization do not fully represent the polarization of the lidar signal and suffer from crosstalk between the two polarization components. In particular, the perpendicular channel suffers from contributions that are not produced by the depolarization of molecules and aerosol. The imperfect polarization of the laser emission contributes to a small signal on the perpendicular channel but is estimated to be much smaller than 1%. Also, the imperfect behavior of the two polarizing beam splitter cubes introduces some crosstalk. Normally, the crosstalk of a polarizing beam splitter cube might be as large as 5%, but the combination of two cubes reduces this to less than 1%. Also, the nonperfect collimation of the optical return signal might contribute. A thorough discussion of the various factors that might contribute to crosstalk, as well as a method to calibrate the receiver with two polarizations, can be found in [17].

However, in the case of the lidar observatory at Concordia Station, the main contribution to the crosstalk is produced by the depolarization of the return signal by the optical viewport. This viewport, which separates the laboratory environment at room temperature (normally between 15 and 20 °C) from the outside air, with temperatures that might be as low as −70 °C, consists of a triple glass construction, with three panes of glass held together in a glazing unit with two insulating air gaps of about 10 cm between two panes. This is necessary to provide sufficient thermal insulation and functions quite well, but apparently, it causes depolarization in the lidar signal which amounts to about 14%.

Starting from the lidar equation

$$S(z) = \frac{h}{2} \frac{C}{z^2} \frac{\beta(z)}{4\pi} exp[-2 \int_0^z \sigma_{ext}(z')dz']$$ (1)

we can express the signals on the two detectors, if we neglect the extinction and only consider the crosstalk as originating from the optical elements (polarizer and viewport), as

$$S_{\parallel}(z) = g_1 \frac{1}{z^2}\beta_{\parallel}(z)(1-CT) \quad \text{and} \quad S_{\perp}(z) = g_2 \frac{1}{z^2}\left(\beta_{\perp}(z) + CT\beta_{\parallel}(z)\right)$$ (2)

where g_1 and g_2 are the gain factors of the two detectors, and CT is the crosstalk from the parallel channel to the perpendicular channel. We neglect the crosstalk from perpendicular to parallel channel.

In order to facilitate the interpretation of the signals and the detection of clouds, we divide both signals by the molecular backscatter coefficient and multiply by z^2 and we get

$$r_{\parallel}(z) = g_1 \frac{\beta_{\parallel}(z)(1-CT)}{\beta_{\text{mol}}(z)} \quad \text{and} \quad r_{\perp}(z) = g_2 \frac{(\beta_{\perp}(z) + CT\beta_{\parallel}(z))}{\beta_{\text{mol}}(z)}$$ (3)

The molecular backscatter coefficient was calculated using local temperature and pressure provided by radio soundings and, where these were not available, from the NCEP (National Centers for Environmental Predictions).

We can normalize these expressions to 1, where no aerosols are present (typically between 26 and 30 km). The normalized expressions become

$$r'_{\parallel}(z) = \frac{r_{\parallel}(z)}{rn_{\parallel}} \quad \text{and} \quad r'_{\perp}(z) = \frac{r_{\perp}(z)}{rn_{\perp}}$$ (4)

where

$$rn_{\parallel} = g_1 \frac{\beta_{\text{mol}\parallel}}{\beta_{\text{mol}}}(1 - CT) \quad \text{and} \quad rn_{\perp} = g_2 \left[\frac{\beta_{\text{mol}\perp}}{\beta_{\text{mol}}} + CT \frac{\beta_{mol\parallel}}{\beta_{\text{mol}}} \right] \tag{5}$$

With some algebra, we can now obtain expressions for R and $\beta_{\perp}$

$$R(z) = \frac{(1 - CT)}{1 + \delta_{\text{mol}}} \left[r'_{\parallel}(z) + r'_{\perp}(z) \frac{\delta_{\text{mol}} + CT}{(1 - CT)} \right] \tag{6}$$

and

$$\beta_{\perp}(z) = \frac{\delta_{\text{mol}} + CT}{1 + \delta_{\text{mol}}} \left[r'_{\perp}(z) - r'_{\parallel}(z) \frac{CT}{\delta_{\text{mol}} + CT} \right] \beta_{\text{mol}}(z) \tag{7}$$

where $\delta_{\text{mol}} = \beta_{\text{mol}\perp}/\beta_{\text{mol}\parallel}$. In our case, using an optical bandpass filter centered on the laser wavelength (532 nm) with an FWHM of 2 nm, δ_{mol} is 0.007 ([18]).

Now, we can see that the crosstalk CT can be written as

$$CT = \frac{\frac{g_1}{g_2} \frac{rn_{\perp}}{rn_{\parallel}} - \delta_{\text{mol}}}{1 + \frac{g_1}{g_2} \frac{rn_{\perp}}{rn_{\parallel}}} \tag{8}$$

The two parameters $rn_{\parallel}$ and $rn_{\perp}$ can be determined from the calibration process for aerosol-free regions, so we only need the ratio of the two gain constants of the two detection channels, which can be determined, e.g., by switching the detectors or by more sophisticated methods ([17]).

After correcting the two channels for extinction and range, two optical parameters can be extracted, taking the crosstalk into account. The backscatter ratio R, defined as the ratio of the total backscatter coefficient and the molecular backscatter coefficient, accounts for the scattering by particles (aerosol) with respect to molecular scattering. This implies that $R = 1$ if no aerosols are present. The second parameter accounts for the depolarization caused by solid particles and can be described by several parameters [19]. The linear volume depolarization is defined as the ratio of the perpendicular backscatter coefficient and the parallel backscatter coefficient, while the aerosol depolarization can be expressed as the ratio of the perpendicular backscatter coefficient and the parallel backscatter coefficient for aerosol only. We use the perpendicular backscatter coefficient $\beta_{\perp}$ as a measure for depolarization to facilitate the comparison with CALIOP data.

The determination of the two optical parameters, R and $\beta_{\perp}$, as well as their errors, allows one to define detection limits and classify the different PSC classes.

2.4. Detection and Classification of PSCs

In a previous work [8], an extensive comparison study of ground-based and quasi-coincident satellite-borne lidar observations of PSCs was performed. To make this comparison, we had to adopt a detection and classification algorithm that follows the same approach and uses the same optical parameters as the v2 CALIOP algorithm (see Figure 7 and [7,20]). This approach seems to be successful and is now also followed by others (see [5]). However, the detection thresholds to distinguish PSCs from background aerosol had to be calculated in a different way. For CALIOP observations, the signal due to background aerosol from measurements is determined from observations at different locations on the same orbit, where no PSCs are present. For the ground-based observations, the background aerosol signal is taken from apparent clear sky observations, which are far less frequent than PSC observations during winter and often have a large time difference with respect to the PSC observations.

Furthermore, statistical errors inherent in the photon-counting process and thus dependent on the altitude and the possible attenuation in the lower troposphere were taken into account to calculate the errors of the optical parameters $u(\beta_{\perp})$ and $u(R)$ and create the dynamic thresholds for detection and classification.
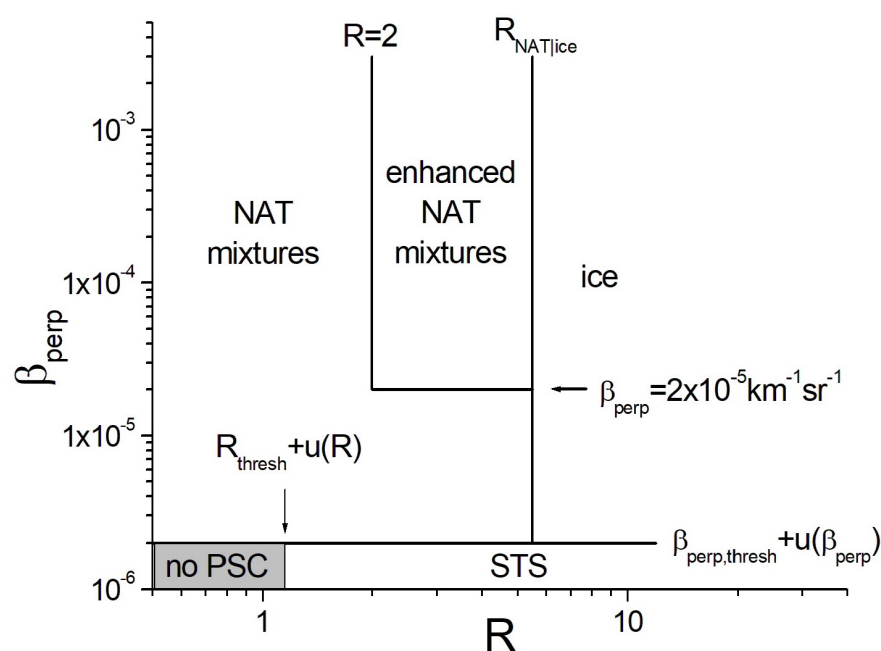
Figure 7. The figure shows the criteria using the backscatter ratio R and the perpendicular backscatter coefficient β_{perp} to classify the different PSC types.

The detection of a PSC is positive if either R or $\beta_\perp$ exceeds the threshold value. It should be noted that the threshold values are not fixed but vary with the altitude due to the variation in the signal-to-noise ratio of the measured parameters. The classification of the PSCs closely follows the criteria established for the CALIOP data and identifies 5 different classes, STSs (Supercooled Ternary Solutions), NAT (Nitric Acid Trihydrate) mixtures, enhanced NAT mixtures, ice, and wave ice. With the term NAT mixtures, we intend mixtures of NAT with STSs and other nonpolarizing particles. PSCs generally consist of external mixtures of different species. The classification is based on the measurement of optical parameters and as such on the average contribution of several species to backscatter coefficient and depolarization. Enhanced NAT particles correspond to NAT with $r_{NAT} < 3$ μm and a volume density of more than 1 $\mu m^3 cm^{-3}$ [20] and corresponds roughly with NAT heterogeneously nucleated in wave ice PSCs. Wave ice PSCs are ice PSCs with $R > 50$. Wave ice seldom occurs above Concordia, since no significant orographic features are present. Also, enhanced NAT has a low occurrence. The main PSC classes observed at Concordia Station are NAT mixtures, STSs, and ice.

3. Results

The Concordia lidar observatory has been active since 2014. Lidar profiles have been recorded during the months of major PSC occurrences, namely from June through September. Usually, two to four profiles are recorded every day, with the exception of prohibitive meteorological conditions, such as storms, precipitation, or strongly absorbing tropospheric clouds. In 2019, both lasers broke down and no data acquisitions were possible. Here, we show the PSC observations performed in 2021 as an example of the seasonal variations in PSC occurrences.

The formation of PSCs is mainly dictated by temperature, since the different kinds of PSCs exist in a limited temperature range (see, e.g., refs. [21–23]). Above a certain threshold temperature, they simply evaporate and cease to exist as solid or liquid particles. On the other hand, the formation processes can follow different pathways depending on temperature history induced by either large synoptic fields or mesoscale features. The upper temperature threshold for PSCs is the formation temperature for NAT (T_{NAT}), which is around 195 K depending on the water vapor and nitric acid mixing ratios, local

pressure, and temperatures [24]. T_{NAT} is the highest PSC formation temperature that is thermodynamically possible, but usually NAT forms at about 2.5–3 K below T_{NAT} [20]. Water ice PSCs have the lowest formation temperature (about 188 K), the so-called frost temperature T_{ice} (see, e.g., ref. [25] or [26] for different methods to calculate the frost point).

The nucleation and growth of the different PSCs have been extensively discussed elsewhere [27]. The abundance of water in the troposphere and stratosphere, with respect to nitric acid, sulfuric acid, and other condensable species, produces ice PSCs when the local temperature is low enough. Homogeneous ice nucleation from SSA (supercooled sulfuric acid) or from STSs occurs typically at T_{ice}-4 K [28–30], while heterogeneous nucleation on NAT particles already occurs below T_{ice} but above T_{ice}-4 K [31,32].

For the formation of NAT particles, several pathways have been proposed [33]. The heterogeneous nucleation on ice particles requires that the temperature be low enough to produce ice PSCs, implying that other formation processes are required for $T > T_{ice}$.

The heterogeneous nucleation on background aerosols containing meteoritic material [34] or other condensation nuclei might occur readily below T_{NAT}. However, the possibility of homogeneous nucleation on STSs was rejected by [30].

Liquid STS droplets, being ternary solutions with a variable stoichiometry, do not form below a definite threshold temperature but rather grow by a continuous uptake of nitric acid by sulfuric acid aerosols, which becomes massive below 195 K [35]. The composition of the STS droplets changes with temperature; while temperature decreases, the HNO_3 concentration increases while the H_2SO_4 concentration decreases.

The formation of PSCs causes a depletion of water and nitric acid in the gas phase, which leads to dehydration and denitrification of the stratosphere.

Ground-Based and CALIOP PSC Observations in 2021

A large part of the ground-based lidar observations at Concordia Station are synchronized with overpasses of the CALIPSO satellite, with an air-borne lidar (CALIOP) on board. CALIPSO was launched in April 2006 as a component of the A-train satellite constellation [36,37]. With an orbit inclination of 98.2°, it provides extensive daily measurement coverage over the polar regions of both hemispheres at up to 82° in latitude. The primary instrument of CALIPSO is CALIOP. CALIOP has extensively been used for observing PSCs [20,38–40].

CALIPSO performs 14 to 15 orbits per day. On average, two of those have a footprint within 300 km of Concordia Station, although very few orbits have a footprint of less than 10 km. A quasi-synchronous observation is obtained by starting the ground-based observation 16 min before the overpass, with a duration of 32 min. Considering the geometries and time difference between the two observations, it seldom occurs that both lidars observe the same airmass at the same time. But, we showed in a previous work [8] that these quasi-coincident observations often had a good agreement for what concerns the detection of PSCs and, albeit with a lesser frequency, they also produced similar classifications. The comparison of observations made by different instruments, in terms of detection and classification, requires that similar algorithms and thresholds be used. Achtert and Tesche [41] reported a study of different classification schemes for PSCs and showed that measurements made by a ground-based lidar but elaborated with different criteria often produced a different outcome. The comparison between ground-based and satellite-borne lidars is even more difficult because the observation geometries and the frequency of data acquisition are very different. For instance, ground-based lidars have to deal with bad weather conditions or the presence of optically thick cirrus clouds, which attenuate the laser beam, while satellite-borne lidar does not have this kind of problem. On the other hand, the satellite-borne lidar observes from a large distance, with an orbit being about 800 km from the surface, while the ground-based lidar is much closer to the observed PSCs. Ground-based lidar always observes the same space, and during polar winter, real clear sky measurements seldom occur. Satellite-borne lidar during each orbit observes both

PSCs and clear sky profiles. This is important for calibration purposes and may introduce major calibration errors for ground-based systems.

Figure 8 shows 264 PSC profiles observed by ground-based lidar and 262 CALIOP profiles. The figure was obtained as follows: the ground-based data were gridded on a 180 m grid, since the CALIOP data have a vertical resolution of 180 m. The color codes identify the different PSC classes as follows: NAT mixtures, STSs, ice, and enhanced NAT mixtures are displayed in green, orange, blue, and red, respectively.

From the global CALIOP data, all overpasses within a latitude–longitude range defined by the coordinates 73.1°S < lat < 77.1°S and 116.33°E < lon < 130.33°E centered on Concordia Station were selected. Then, for each overpass, the profile with the nearest footprint with respect to Concordia Station was used to extract the PSC classification as provided in the PSC special product data set to be compared with the quasi-coincident ground-based profile, as can be observed in Figure 8. The average distance of the CALIOP footprints was 146 km, while the largest distance was 300 km. Instead of taking the nearest profile, other approaches were considered but rejected, based on a previous study of a great number of CALIOP tracks (see [8]). For instance, one might average the optical parameters of several CALIOP profiles during an overpass, but this would invariably produce average values for these parameters, leading to a predominant classification of NAT mixtures at the cost of STS and ice. The same would happen if one would classify the PSCs observed during a CALIOP overpass as the most frequently observed PSC class during that overpass. The overall agreement between ground-based and CALIOP data is remarkable and is mostly due to the fact that the PSC fields above Concordia Station consist of rather extended and homogeneous clouds, as demonstrated previously [8].
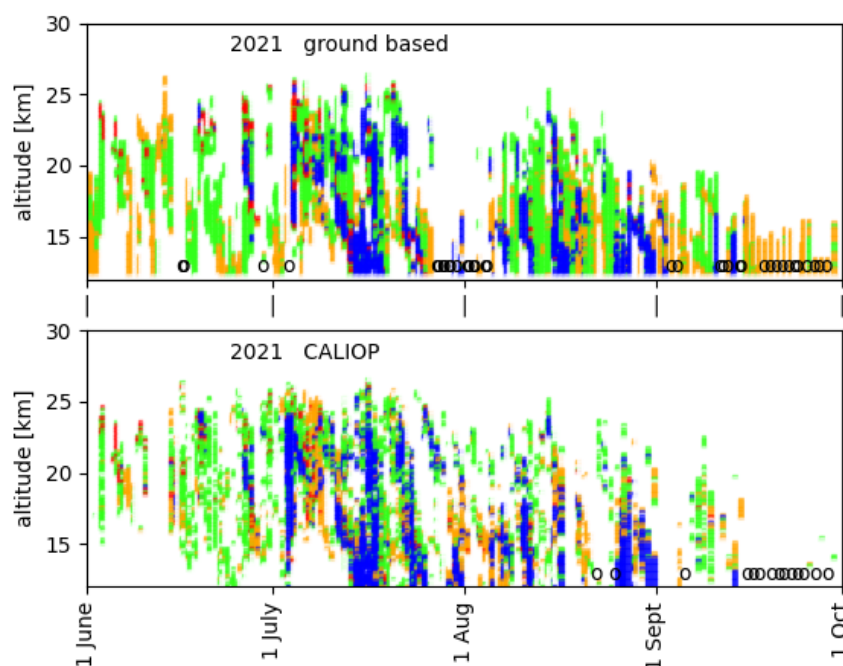

Figure 8. The figure shows the PSCs observed by lidar over Concordia Station in 2021. The upper level shows the ground-based observations, while the lower panel represents the CALIOP data, considering a latitude–longitude range defined by the coordinates 73.1°S < lat < 77.1°S and 116.33°E < lon < 130.33°E centered on Concordia Station. The color codes indicate the different PSC classes; orange stands for STSs, green for NAT mixtures, blue for ice, and red for enhanced NAT mixtures. The small circles indicate that a measurement is available but no PSCS were observed.

4. Discussion

First of all, the remarkable agreement between ground-based and satellite-borne lidar has to be commented on. Notwithstanding the different observing geometry of both lidars, as well as comparing observations of air masses at different times and locations, the

agreement shown in Figure 8 is rather good. We must note, however, that the ground-based lidar in general detects more PSCs, probably due to its better signal-to-noise ratio.

In a previous study [8], a large number of quasi-coincident lidar observations by the ground-based lidar at Concordia Station and the satellite-borne CALIOP lidar demonstrated that in almost 80% of all observations, both lidars observe PSCs or do not observe PSCs when the observations were within a certain time and distance. In the other 20%, only one of the two lidars observed PSCs and the other did not. This is mainly due to the fact that Concordia Station is located on a plateau with few orographic features. This implies that the temperature is quite homogeneous over a large area. As a result, the PSC fields are also expected to be rather homogeneous over extended ranges, as was demonstrated by an analysis of CALIOP tracks passing at distances of a few hundred kilometers from Concordia Station [8]. The formation of PSCs due to orographic wave activity, occurring primarily over the Antarctic Peninsula, is practically absent on the plateau [20]. We tried to further explore the representativeness of the Concordia PSC observations for the whole Antarctic Plateau. Figure 9 was conceived in the same way as Figure 8 but considering a latitude–longitude range for the CALIOP data, defined by the coordinates 73.1°S < lat < 77.1°S and 100°E < lon < 150°E centered on Concordia Station. This extended zonal area increases the number of CALIOP profiles considered from 262 to 646, while the average distance becomes 360 km, and the maximum distance is 815 km. The agreement between ground-based and CALIOP observations is still reasonably good and confirms that Concordia Station has good approximation that is representative of the Antarctic Plateau. This confirms the importance of Concordia Station as a long time series observatory of PSCs in Antarctica while considering that CALIOP was decommissioned in 2023.
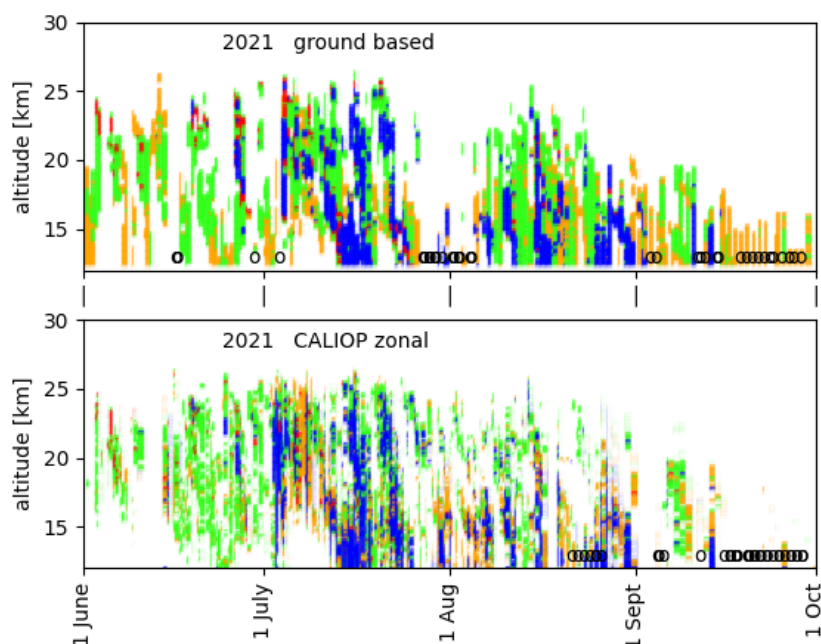

Figure 9. The figure shows the PSCs observed by lidar over Concordia Station in 2021. The upper level shows the ground-based observations, while the lower panel represents the CALIOP data considering a latitude–longitude range defined by the coordinates 73.1°S < lat < 77.1°S and 100°E < lon < 150° E centered on Concordia Station. The color codes indicate the different PSC classes; orange stands for STSs, green for NAT mixtures, blue for ice, and red for enhanced NAT mixtures. The small circles indicate that a measurement is available, but no PSCS were observed.

The 2021 data are peculiar from a certain point of view; the ubiquitous presence of ice PSCs during most of the winter is a result of the cold temperatures in the polar vortex in 2021. Figure 10 shows a time series of when the air is colder than 195 K at 450 K potential temperature obtained from the Climate Prediction Center website (https:

//www.cpc.ncep.noaa.gov/ (accessed on 11 May 2024)) for 2021. It is evident that the 2021 SH vortex covered a larger area than on average. Furthermore, the 2021 polar stratospheric vortex was stable with consistently cold temperatures [42]. Weaker than usual amplitudes of planetary-scale Rossby waves in the September–October period helped maintain a strong vortex and led to below-average Antarctic ozone columns in late Australian spring and early summer. [42].
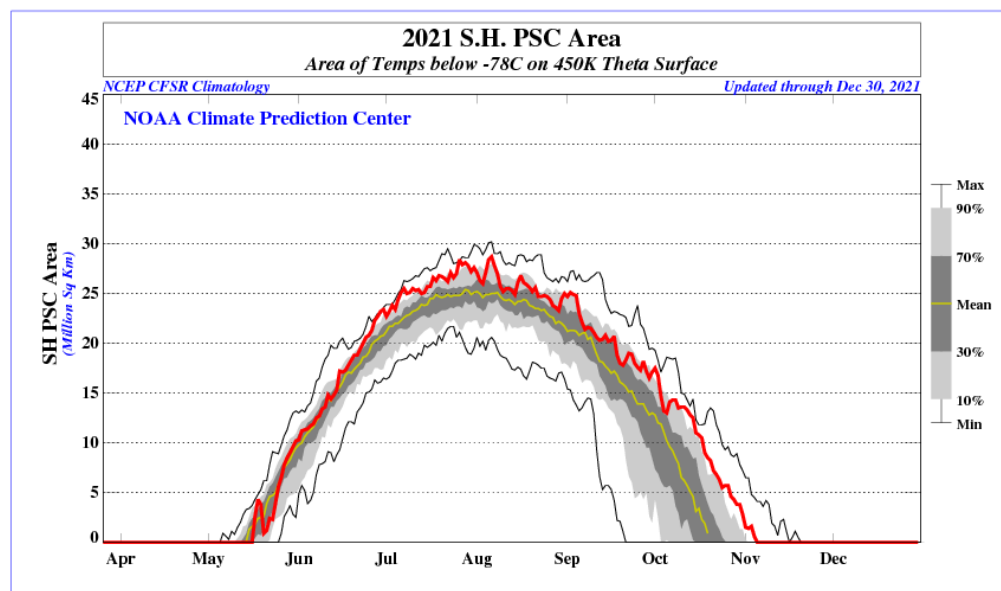

Figure 10. The figure shows the PSC area of the southern hemisphere in 2021 at a potential temperature of 450 K. The red line shows the PSC area in the SH 2021, the black lines correspond with the minimum and maximum values recorded in the previous 10 years. The yellow line stands for the mean value in the preceding 10 years

Since ice PSCs are easy to detect, have a large backscatter ratio, and are also easily classified for the same reason, the probability that both lidars detect them is larger than, for instance, the STSs of NAT mixtures, having an average backscatter ratio and small depolarization. Thus, the presence of many ice PSCs enhances the agreement between the observations of both lidars.

PSC formation is strongly related to the local temperature. In Figure 11, the areas with temperatures below T_{NAT}-3K are shown in green and indicate where and when PSCs are likely to be formed based on temperature only. The red areas correspond to temperatures below the frost temperature of ice and indicate where ice PSCs are expected, but we must bear in mind that NAT and STSs might also be observed at these temperatures. The local temperatures were obtained by merging radio sonde data recorded at Concordia Station, with a vertical resolution of about 5 m, with NCEP data with a vertical resolution of about 2 km. Note that the radio sondes are released once per day on a weather balloon from Concordia Station. These weather balloons explode at a certain altitude, which varies from about 17 km during winter up to more than 30 km during summer. The merged temperatures thus mainly rely on radio sonde measurements and use NCEP data for the upper part of the lidar measurements. Subsequently, the merged temperature is gridded on a 180 m vertical scale to conform with the lidar data. The formation temperatures were calculated from local pressure, water vapor, and nitric acid mixing ratios obtained from MLS data with a vertical resolution of about 1 km and were also gridded on a 180 m vertical scale. MLS data have a footprint of 5 × 200 km (cross-track and along-track, respectively).
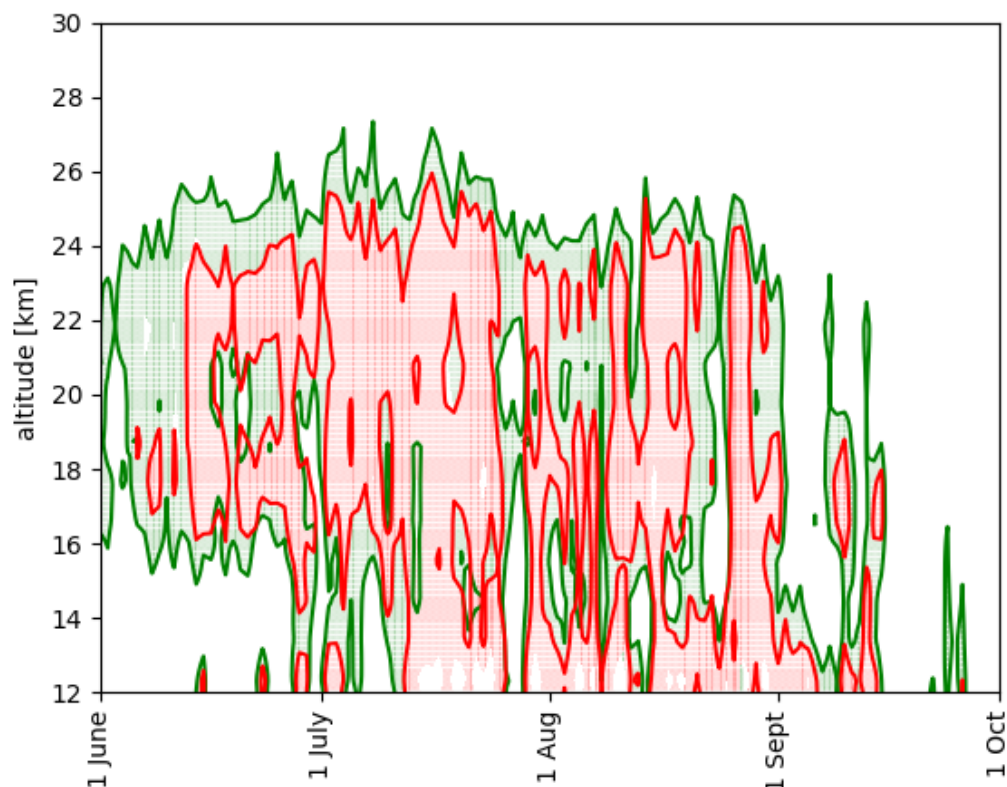
Figure 11. The figure shows the frost temperature (in red) and the NAT formation temperature minus 3 K to show where ice PSCs, NAT and STSs PSCs, respectively, are probably formed. The green contours indicate where the local temperature is below the formation temperature of NAT minus 3 K. The formation temperatures were calculated from local pressure and water vapor and nitric acid mixing ratios were obtained from MLS data.

In Figures 8 and 11, we can observe from the reporting of the PSC observations and temperature fields, respectively, during 2021 that PSCs are seldom observed when the local temperature exceeds T_{NAT}-3K. For example, during the first 10 days of June, temperatures below 14–16 km are too high to allow the formation of PSCs. Also, very few PSCs can be observed above 26 km, where the temperature is too high. The red contours, indicating T_{ice} enclose favorable conditions for ice PSC formation, and it can be observed that ice PSCs are observed below T_{ice}, and it is clear that $T < T_{ice}$ is a necessary condition but not sufficient condition for ice PSC formation. With respect to previous years, the 2021 polar vortex was rather cold, as can be seen in Figure 11, where large areas of temperatures below T_{ice} can be observed. Until the middle of June, temperatures are too high for ice PSCs to form, and we mainly see NAT mixtures, where NAT is formed by heterogeneous nucleation on background aerosol or other condensation nuclei. In July and August, ice PSCs are often observed in correspondence with temperatures below 185 K. The formation of ice PSCs leads to dehydration, which can also be observed in MLS measurements of the water vapor mixing ratio (see Figure 12) . At temperatures below T_{ice}, the coexistence of ice, NAT mixtures, and STSs can be observed.

The observation of STSs in September by the ground-based lidar is somewhat surprising considering the temperature maps. PSCs are seldom observed by CALIOP in September above Concordia Station [8], but this may be due to a minor sensitivity with respect to the ground-based lidar. On the other hand, it might be an instrumental effect due to the presence of sunlight causing baseline fluctuations, which have a major effect on the weaker depolarized signal.
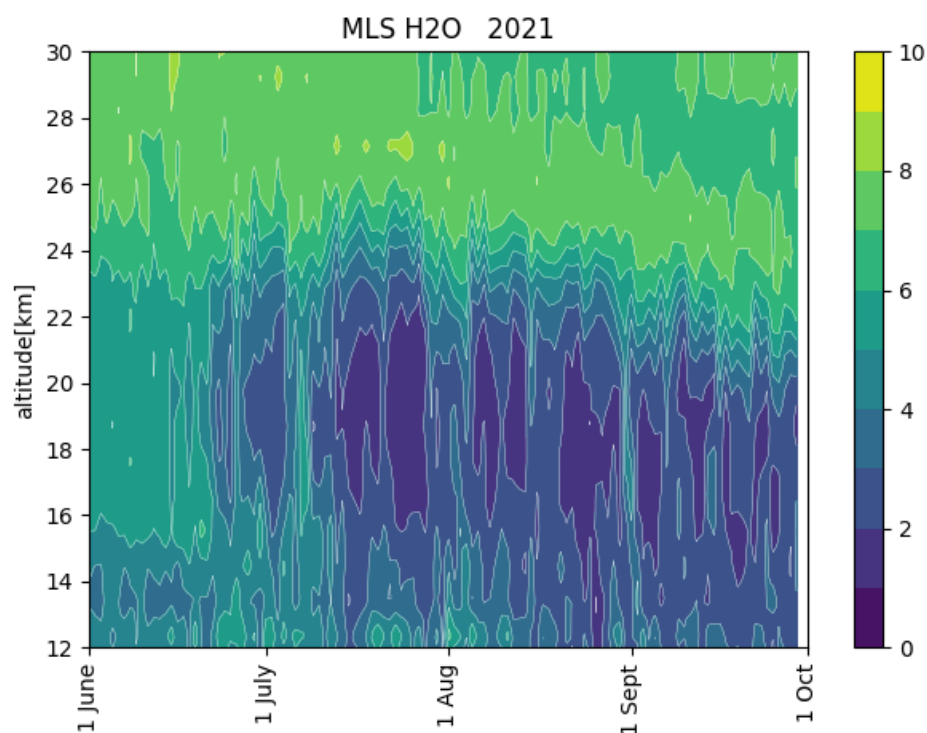
Figure 12. The figure shows the water vapor mixing ratio in ppm as observed by MLS in 2021.

Abbreviations

The following abbreviations are used in this manuscript:

PSC	Polar Stratospheric Cloud
LIDAR	LIght Detecting And Ranging
CALIOP	Cloud-Aerosol Lidar with Orthogonal Polarization
CALIPSO	Cloud-Aerosol Lidar and Infrared Pathfinder Satellite Observation
NAT	Nitric Acid Trihydrate
STS	Supercooled Ternary Solution
MLS	Microwave Limb Sounder
PNRA	Programma Nazionale delle Ricerche in Antartide
NDACC	Network for the Detection of Stratospheric Change
NCEP	National Centers for Environmental Prediction
ERA-5	ECMWF ReAnalysis version 5
ECMWF	European Centre for Medium-Range Weather Forecasts

References

1. Sassen, K. The Polarization Lidar Technique for Cloud Research: A Review and Current Assessment. *Bull. Am. Meteorol. Soc.* **1991**, *72*, 1848–1866. [CrossRef]
2. Krueger, B.C. Observations of polar stratospheric clouds in the Arctic winter 1989 at 79 N. *Geophys. Res. Lett.* **1990**, *17*, 365–368. [CrossRef]
3. Fiocco, G.; Cacciani, M.; Di Girolamo, P.; Fua, D. Stratospheric clouds at South-Pole during 1988 1. Results of lidar observations and their relationship to temperature. *J. Geophys. Res. Atmos.* **1992**, *97*, 5939–5946. [CrossRef]
4. Stefanutti, L.; Morandi, M.; Guasta, M.D.; Godin, S.; Megie, G.; Brechet, J.; Piquard, J. Polar stratospheric cloud observations over the Antarctic continent at Dumont d'Urville. *J. Geophys. Res. Atmos.* **1991**, *96*, 12975–12987. [CrossRef]
5. Tencé, F.; Jumelet, J.; Bouillon, M.; Cugnet, D.; Bekki, S.; Safieddine, S.; Keckhut, P.; Sarkissian, A. 14 years of lidar measurements of polar stratospheric clouds at the French Antarctic station Dumont d'Urville. *Atmos. Chem. Phys.* **2023**, *23*, 431–451. [CrossRef]
6. Adriani, A.; Massoli, P.; Di Donfrancesco, G.; Cairo, F.; Moriconi, M.; Snels, M. Climatology of polar stratospheric clouds based on lidar observations from 1993 to 2001 over McMurdo Station, Antarctica. *J. Geophys. Res. Atmos.* **2004**, *109*, D24211. [CrossRef]
7. Snels, M.; Scoccione, A.; Di Liberto, L.; Colao, F.; Pitts, M.; Poole, L.; Deshler, T.; Cairo, F.; Cagnazzo, C.; Fierli, F. Comparison of Antarctic polar stratospheric cloud observations by ground-based and spaceborne lidars and relevance for chemistry-climate Models. *Atmos. Chem. Phys.* **2019**, *19*, 955–972. [CrossRef]
8. Snels, M.; Colao, F.; Cairo, F.; Shuli, I.; Scoccione, A.; De Muro, M.; Pitts, M.; Poole, L.; Di Liberto, L. Quasi-coincident observations of polar stratospheric clouds by ground-based lidar and CALIOP at Concordia (Dome C, Antarctica) from 2014 to 2018. *Atmos. Chem. Phys.* **2021**, *21*, 2165–2178. [CrossRef]
9. Snels, M.; Cairo, F.; Di Liberto, L.; Scoccione, A.; Bracaglia, M.; Deshler, T. Comparison of Coincident Optical Particle Counter and Lidar Measurements of Polar Stratospheric Clouds Above McMurdo (77.85°S, 166.67°E) from 1994 to 1999. *J. Geophys. Res. Atmos.* **2021**, *126*, e2020JD033572. [CrossRef]
10. Cairo, F.; Deshler, T.; Di Liberto, L.; Scoccione, A.; Snels, M. A study of optical scattering modelling for mixed-phase polar stratospheric clouds. *Atmos. Meas. Tech.* **2023**, *16*, 419–431. [CrossRef]
11. Tesche, M.; Achtert, P.; Pitts, M.C. On the best locations for ground-based polar stratospheric cloud (PSC) observations. *Atmos. Chem. Phys.* **2021**, *21*, 505–516. [CrossRef]
12. Di Liberto, L.; Cairo, F.; Fierli, F.; Di Donfrancesco, G.; Viterbini, M.; Deshler, T.; Snels, M. Observation of polar stratospheric clouds over McMurdo (77.85°S, 166.67°E) (2006–2010). *J. Geophys. Res. Atmos.* **2014**, *119*, 5528–5541. [CrossRef]
13. Klett, J. Lidar Inversion with Variable Backscatter/Extinction Ratios. *Appl. Opt.* **1985**, *24*, 1638–1643. [CrossRef] [PubMed]
14. Young, S.A.; Vaughan, M.A. The Retrieval of Profiles of Particulate Extinction from Cloud-Aerosol Lidar Infrared Pathfinder Satellite Observations (CALIPSO) Data: Algorithm Description. *J. Atmos. Ocean. Technol.* **2009**, *26*, 1105–1119. [CrossRef]
15. Böckmann, C.; Ritter, C. Properties of Polar Stratospheric Clouds over the European Arctic from Ground-Based Lidar. In Proceedings of the 30th International Laser Radar Conference, Big Sky, MT, USA, 26 June–1 July 2022; Springer: Berlin/Heidelberg, Germany, 2023; pp. 325–332. [CrossRef]
16. Gobbi, G. Lidar estimation of stratospheric aerosol properties—Surface, volume, and extinction to backscatter ratio. *J. Geophys. Res. Atmos.* **1995**, *100*, 11219–11235. [CrossRef]
17. Snels, M.; Cairo, F.; Colao, F.; Di Donfrancesco, G. Calibration method for depolarization lidar measurements. *Int. J. Remote Sens.* **2009**, *30*, 5725–5736. [CrossRef]
18. Behrendt, A.; Nakamura, T. Calculation of the calibration constant of polarization lidar and its dependency on atmospheric temperature. *Opt. Express* **2002**, *10*, 805–817. [CrossRef]
19. Cairo, F.; Donfrancesco, G.D.; Adriani, A.; Pulvirenti, L.; Fierli, F. Comparison of various linear depolarization parameters measured by lidar. *Appl. Opt.* **1999**, *38*, 4425–4432. [CrossRef] [PubMed]

20. Pitts, M.C.; Poole, L.R.; Gonzalez, R. Polar stratospheric cloud climatology based on CALIPSO spaceborne lidar measurements from 2006–2017. *Atmos. Chem. Phys.* **2018**, *2018*, 10881–10913. [CrossRef]

21. Tabazadeh, A.; Toon, O.; Hamill, P. Freezing behaviour of stratospheric sulfate aerosols inferred from trajectory studies. *Geophys. Res. Lett.* **1995**, *22*, 1725–1728. [CrossRef]

22. Larsen, N.; Knudsen, B.; Rosen, J.; Kjome, N.; Neuber, R.; Kyro, E. Temperature histories in liquid and solid polar stratospheric cloud formation. *J. Geophys. Res. Atmos.* **1997**, *102*, 23505–23517. [CrossRef]

23. Toon, O.; Tabazadeh, A.; Browell, E.; Jordan, J. Analysis of lidar observations of Arctic polar stratospheric clouds during January 1989. *J. Geophys. Res. Atmos.* **2000**, *105*, 20589–20615. [CrossRef]

24. Hanson, D.; Mauersberger, K. Laboratory studies of the nitric acid trihydrate: Implications for the south polar stratosphere. *Geophys. Res. Lett.* **1988**, *15*, 855–858. [CrossRef]

25. Murphy, D.M.; Koop, T. Review of the vapour pressures of ice and supercooled water for atmospheric applications. *Quart. J. R. Meteorol. Soc.* **2005**, *131*, 1539–1565. [CrossRef]

26. Romps, D.M. Accurate Expressions for the Dewpoint and Frost Point Derived from the Rankine–Kirchhoff Approximations. *J. Atmos. Sci.* **2021**, *78*, 2113–2116. [CrossRef]

27. Tritscher, I.; Pitts, M.C.; Poole, L.R.; Alexander, S.P.; Cairo, F.; Chipperfield, M.P.; Grooß, J.U.; Höpfner, M.; Lambert, A.; Luo, B.; et al. Polar Stratospheric Clouds: Satellite Observations, Processes, and Role in Ozone Depletion. *Rev. Geophys.* **2021**, *59*, e2020RG000702. [CrossRef]

28. Carslaw, K.S.; Wirth, M.; Tsias, A.; Luo, B.P.; Dörnbrack, A.; Leutbecher, M.; Volkert, H.; Renger, W.; Bacmeister, J.T.; Peter, T. Particle microphysics and chemistry in remotely observed mountain polar stratospheric clouds. *J. Geophys. Res. Atmos.* **1998**, *103*, 5785–5796. [CrossRef]

29. Koop, T.; Ng, H.P.; Molina, L.T.; Molina, M.J. A New Optical Technique to Study Aerosol Phase Transitions: The Nucleation of Ice from H_2SO_4 Aerosols. *J. Phys. Chem. A* **1998**, *102*, 8924–8931. [CrossRef]

30. Koop, T.; Biermann, U.; Raber, W.; Luo, B.; Crutzen, P.; Peter, T. Do stratospheric droplets freeze above the ice frost point? *Geophys. Res. Lett.* **1995**, *22*, 917–920. [CrossRef]

31. Koop, T.; Carslaw, K.S.; Peter, T. Thermodynamic stability and phase transitions of PSC particles. *Geophys. Res. Lett.* **1997**, *24*, 2199–2202. [CrossRef]

32. Peter, T. Microphysics and heterogeneous chemistry of polar stratospheric clouds. *Annu. Rev. Phys. Chem.* **1997**, *48*, 785–822. [CrossRef] [PubMed]

33. Peter, T.; Grooß, J.U. Polar Stratospheric Clouds and Sulfate Aerosol Particles: Microphysics, Denitrification and Heterogeneous Chemistry. In *Stratospheric Ozone Depletion and Climate Change*; The Royal Society of Chemistry: London, UK, 2012; pp. 108–144. [CrossRef]

34. Curtius, J. Observations of meteoritic material and implications for aerosol nucleation in the winter Arctic lower stratosphere derived from in situ particle measurements. *Atmos. Chem. Phys. Discuss.* **2005**, *5*, 5039–5080.

35. Carslaw, K.; Luo, B.; Peter, T. An analytic expression for the composition of acqueous HNO_3-H_2SO_4 stratospheric aerosols including gas-phase removal of HNO_3. *Geophys. Res. Lett.* **1995**, *22*, 1877–1880. [CrossRef]

36. Stephens, G.L.; Vane, D.G.; Boain, R.J.; Mace, G.G.; Sassen, K.; Wang, Z.; Illingworth, A.J.; O'Connor, E.J.; Rossow, W.B.; Durden, S.L.; et al. The CloudSat mission and the A-Train: A new dimension of space-based observations of clouds and precipitation. *Bull. Am. Meteorol. Soc.* **2002**, *83*, 1771–1790. [CrossRef]

37. Stephens, G.; Winker, D.; Pelon, J.; Trepte, C.; Vane, D.; Yuhas, C.; L'Ecuyer, T.; Lebsock, M. CloudSat and CALIPSO within the A-Train: Ten Years of Actively Observing the Earth System. *Bull. Am. Meteorol. Soc.* **2018**, *99*, 569–581. [CrossRef]

38. Pitts, M.C.; Poole, L.R.; Thomason, L.W. CALIPSO polar stratospheric cloud observations: Second-generation detection algorithm and composition discrimination. *Atmos. Chem. Phys.* **2009**, *9*, 7577–7589. [CrossRef]

39. Pitts, M.C.; Poole, L.R.; Dörnbrack, A.; Thomason, L.W. The 2009–2010 Arctic polar stratospheric cloud season: A CALIPSO perspective. *Atmos. Chem. Phys.* **2011**, *11*, 2161–2177. [CrossRef]

40. Pitts, M.C.; Poole, L.R.; Lambert, A.; Thomason, L.W. An assessment of CALIOP polar stratospheric cloud composition classification. *Atmos. Chem. Phys.* **2013**, *13*, 2975–2988. [CrossRef]

41. Achtert, P.; Tesche, M. Assessing lidar-based classification schemes for polar stratospheric clouds based on 16 years of measurements at Esrange, Sweden. *J. Geophys. Res. Atmos.* **2014**, *119*, 1386–1405. [CrossRef]

42. Clem, K.R.; Raphael, M.N.; Adusumilli, S.; Baiman, R.; Banwell, A.F.; Barreira, S.; Beadling, R.L.; Colwell, S.; Coy, L.; Datta, R.T.; et al. Antarctica and the Southern Ocean. *Bull. Am. Meteorol. Soc.* **2022**, *103*, S307–S340. [CrossRef]